Biomedical Optics EXPRESS

Simultaneous real-time imaging of the ocular anterior segment including the ciliary muscle during accommodation

Yilei Shao,[1,2,5] Aizhu Tao,[1,2,5] Hong Jiang,[1] Meixiao Shen,[2] Jianguang Zhong,[1,3] Fan Lu,[2] and Jianhua Wang[1,4,*]

[1] *Bascom Palmer Eye Institute, University of Miami, Miami, FL, 33136, USA*
[2] *School of Ophthalmology and Optometry, Wenzhou Medical College, Wenzhou, Zhejiang, China*
[3] *Department of Ophthalmology, Hangzhou First People's Hospital, Hangzhou, Zhejiang, China*
[4] *Electrical and Computer Engineering, University of Miami, Miami, FL, USA*
[5] *These authors contributed equally to this work*
**jwang3@med.miami.edu*

Abstract: We demonstrated a novel approach of imaging the anterior segment including the ciliary muscle using combined and synchronized two spectral domain optical coherence tomography devices (SD-OCT). In one SD-OCT, a Complementary Metal-Oxide-Semiconductor Transistor (CMOS) camera and an alternating reference arm was used to image the anterior segment from the cornea to the lens. Another SD-OCT for imaging the ciliary muscle was equipped with a light source with a center wavelength of 1,310 nm and a bandwidth of 75 nm. Repeated measurements were performed under relaxed and 4.00 D accommodative stimulus states in six eyes from 6 subjects. We also imaged dynamic changes in the anterior segment in one eye during accommodation. The biometry of the anterior segment and the ciliary muscle was obtained. The combined system appeared to be capable to simultaneously real-time image the biometry of the anterior segment, including the ciliary muscle, *in vivo* during accommodation.

OCIS codes: (170.4500) Optical coherence tomography; (170.3880) Medical and biological imaging; (170.4580) Optical diagnostics for medicine; (330.4460) Ophthalmic optics and devices; (330.7322) Visual optics, accommodation.

References and links

1. H. von Helmholtz, "Uber die akkommodation des auges," Arch. Ophthalmol. **1**, 1–74 (1855).
2. D. A. Atchison, "Accommodation and presbyopia," Ophthalmic Physiol. Opt. **15**(4), 255–272 (1995).
3. M. T. Pardue and J. G. Sivak, "Age-related changes in human ciliary muscle," Optom. Vis. Sci. **77**(4), 204–210 (2000).
4. S. Tamm, E. Tamm, and J. W. Rohen, "Age-related changes of the human ciliary muscle. A quantitative morphometric study," Mech. Ageing Dev. **62**(2), 209–221 (1992).
5. H. J. Wyatt, "Application of a simple mechanical model of accommodation to the aging eye," Vision Res. **33**(5-6), 731–738 (1993).
6. L. Stark, "Presbyopia in light of accommodation," Am. J. Optom. Physiol. Opt. **65**(5), 407–416 (1988).
7. S. A. Strenk, L. M. Strenk, and J. F. Koretz, "The mechanism of presbyopia," Prog. Retin. Eye Res. **24**(3), 379–393 (2005).
8. C. Du, M. Shen, M. Li, D. Zhu, M. R. Wang, and J. Wang, "Anterior segment biometry during accommodation imaged with ultralong scan depth optical coherence tomography," Ophthalmology **119**(12), 2479–2485 (2012).
9. P. S. Yan, H. T. Lin, Q. L. Wang, and Z. P. Zhang, "Anterior segment variations with age and accommodation demonstrated by slit-lamp-adapted optical coherence tomography," Ophthalmology **117**(12), 2301–2307 (2010).
10. M. Shen, L. Cui, M. Li, D. Zhu, M. R. Wang, and J. Wang, "Extended scan depth optical coherence tomography for evaluating ocular surface shape," J. Biomed. Opt. **16**(5), 056007 (2011).
11. Y. Yuan, F. Chen, M. Shen, F. Lu, and J. Wang, "Repeated measurements of the anterior segment during accommodation using long scan depth optical coherence tomography," Eye Contact Lens **38**(2), 102–108 (2012).

#180835 - $15.00 USD Received 10 Dec 2012; revised 14 Feb 2013; accepted 18 Feb 2013; published 21 Feb 2013

12. L. A. Lossing, L. T. Sinnott, C. Y. Kao, K. Richdale, and M. D. Bailey, "Measuring changes in ciliary muscle thickness with accommodation in young adults," Optom. Vis. Sci. **89**(5), 719–726 (2012).
13. A. L. Sheppard and L. N. Davies, "The effect of ageing on in vivo human ciliary muscle morphology and contractility," Invest. Ophthalmol. Vis. Sci. **52**(3), 1809–1816 (2011).
14. K. Richdale, M. D. Bailey, L. T. Sinnott, C. Y. Kao, K. Zadnik, and M. A. Bullimore, "The effect of phenylephrine on the ciliary muscle and accommodation," Optom. Vis. Sci. **89**(10), e1507–e1511 (2012).
15. H. Furukawa, H. Hiro-Oka, N. Satoh, R. Yoshimura, D. Choi, M. Nakanishi, A. Igarashi, H. Ishikawa, K. Ohbayashi, and K. Shimizu, "Full-range imaging of eye accommodation by high-speed long-depth range optical frequency domain imaging," Biomed. Opt. Express **1**(5), 1491–1501 (2010).
16. M. Gora, K. Karnowski, M. Szkulmowski, B. J. Kaluzny, R. Huber, A. Kowalczyk, and M. Wojtkowski, "Ultra high-speed swept source OCT imaging of the anterior segment of human eye at 200 kHz with adjustable imaging range," Opt. Express **17**(17), 14880–14894 (2009).
17. B. Potsaid, B. Baumann, D. Huang, S. Barry, A. E. Cable, J. S. Schuman, J. S. Duker, and J. G. Fujimoto, "Ultrahigh speed 1050nm swept source/Fourier domain OCT retinal and anterior segment imaging at 100,000 to 400,000 axial scans per second," Opt. Express **18**(19), 20029–20048 (2010).
18. I. Grulkowski, J. J. Liu, B. Potsaid, V. Jayaraman, C. D. Lu, J. Jiang, A. E. Cable, J. S. Duker, and J. G. Fujimoto, "Retinal, anterior segment and full eye imaging using ultrahigh speed swept source OCT with vertical-cavity surface emitting lasers," Biomed. Opt. Express **3**(11), 2733–2751 (2012).
19. C. Zhou, J. Wang, and S. Jiao, "Dual channel dual focus optical coherence tomography for imaging accommodation of the eye," Opt. Express **17**(11), 8947–8955 (2009).
20. C. Dai, C. Zhou, S. Fan, Z. Chen, X. Chai, Q. Ren, and S. Jiao, "Optical coherence tomography for whole eye segment imaging," Opt. Express **20**(6), 6109–6115 (2012).
21. C. Du, D. Zhu, M. Shen, M. Li, M. R. Wang, and J. Wang, "Novel optical coherence tomography for imaging the entire anterior segment of the eye," Invest. Ophthalmol. Vis. Sci. **52**, ARVO E-Abstract 3023 (2011).
22. M. Ruggeri, S. R. Uhlhorn, C. De Freitas, A. Ho, F. Manns, and J. M. Parel, "Imaging and full-length biometry of the eye during accommodation using spectral domain OCT with an optical switch," Biomed. Opt. Express **3**(7), 1506–1520 (2012).
23. T. Ide, J. Wang, A. Tao, T. Leng, G. D. Kymionis, T. P. O'Brien, and S. H. Yoo, "Intraoperative use of three-dimensional spectral-domain optical coherence tomography," Ophthalmic Surg. Lasers Imaging **41**(2), 250–254 (2010).
24. T. Leng, B. J. Lujan, S. H. Yoo, and J. Wang, "Three-dimensional spectral domain optical coherence tomography of a clear corneal cataract incision," Ophthalmic Surg. Lasers Imaging **39**(4 Suppl), S132–S134 (2008).
25. American National Standards Institute, "American national standard for safe use of lasers," in Laser Institute of America (Orlando, FL, 2000), pp. 45–49.
26. S. Ortiz, P. Pérez-Merino, E. Gambra, A. de Castro, and S. Marcos, "In vivo human crystalline lens topography," Biomed. Opt. Express **3**(10), 2471–2488 (2012).
27. S. Ortiz, P. Pérez-Merino, N. Alejandre, E. Gambra, I. Jimenez-Alfaro, and S. Marcos, "Quantitative OCT-based corneal topography in keratoconus with intracorneal ring segments," Biomed. Opt. Express **3**(5), 814–824 (2012).
28. D. Siedlecki, A. de Castro, E. Gambra, S. Ortiz, D. Borja, S. Uhlhorn, F. Manns, S. Marcos, and J. M. Parel, "Distortion correction of OCT images of the crystalline lens: gradient index approach," Optom. Vis. Sci. **89**(5), E709–E718 (2012).
29. S. Ortiz, D. Siedlecki, I. Grulkowski, L. Remon, D. Pascual, M. Wojtkowski, and S. Marcos, "Optical distortion correction in optical coherence tomography for quantitative ocular anterior segment by three-dimensional imaging," Opt. Express **18**(3), 2782–2796 (2010).
30. S. Ortiz, D. Siedlecki, L. Remon, and S. Marcos, "Optical coherence tomography for quantitative surface topography," Appl. Opt. **48**(35), 6708–6715 (2009).
31. C. Du, J. Wang, L. Cui, M. Shen, and Y. Yuan, "Vertical and horizontal corneal epithelial thickness profiles determined by ultrahigh resolution optical coherence tomography," Cornea **31**(9), 1036–1043 (2012).
32. S. R. Uhlhorn, F. Manns, H. Tahi, P. O. Rol, and J.-M. A. Parel, "Corneal group refractive index measurement using low-coherence interferometry," Proc. SPIE **3246**, 14–21 (1998).
33. D. A. Atchison and G. Smith, "Chromatic dispersion of the ocular media of human eyes," J. Opt. Soc. Am. A **22**(1), 29–37 (2005).
34. S. R. Uhlhorn, D. Borja, F. Manns, and J. M. Parel, "Refractive index measurement of the isolated crystalline lens using optical coherence tomography," Vision Res. **48**(27), 2732–2738 (2008).
35. M. D. Bailey, L. T. Sinnott, and D. O. Mutti, "Ciliary body thickness and refractive error in children," Invest. Ophthalmol. Vis. Sci. **49**(10), 4353–4360 (2008).
36. I. Grulkowski, M. Gora, M. Szkulmowski, I. Gorczynska, D. Szlag, S. Marcos, A. Kowalczyk, and M. Wojtkowski, "Anterior segment imaging with Spectral OCT system using a high-speed CMOS camera," Opt. Express **17**(6), 4842–4858 (2009).
37. A. L. Sheppard and L. N. Davies, "In vivo analysis of ciliary muscle morphologic changes with accommodation and axial ametropia," Invest. Ophthalmol. Vis. Sci. **51**(12), 6882–6889 (2010).
38. M. V. Sarunic, S. Asrani, and J. A. Izatt, "Imaging the ocular anterior segment with real-time, full-range Fourier-domain optical coherence tomography," Arch. Ophthalmol. **126**(4), 537–542 (2008).

39. S. A. Strenk, J. L. Semmlow, L. M. Strenk, P. Munoz, J. Gronlund-Jacob, and J. K. DeMarco, “Age-related changes in human ciliary muscle and lens: a magnetic resonance imaging study,” Invest. Ophthalmol. Vis. Sci. **40**(6), 1162–1169 (1999).
40. A. P. Beers and G. L. van der Heijde, “Age-related changes in the accommodation mechanism,” Optom. Vis. Sci. **73**(4), 235–242 (1996).
41. A. P. Beers and G. L. Van Der Heijde, “In vivo determination of the biomechanical properties of the component elements of the accommodation mechanism,” Vision Res. **34**(21), 2897–2905 (1994).
42. M. A. Croft, A. Glasser, G. Heatley, J. McDonald, T. Ebbert, D. B. Dahl, N. V. Nadkarni, and P. L. Kaufman, “Accommodative ciliary body and lens function in rhesus monkeys, I: normal lens, zonule and ciliary process configuration in the iridectomized eye,” Invest. Ophthalmol. Vis. Sci. **47**(3), 1076–1086 (2006).
43. S. Jeon, W. K. Lee, K. Lee, and N. J. Moon, “Diminished ciliary muscle movement on accommodation in myopia,” Exp. Eye Res. **105**, 9–14 (2012).
44. M. A. Croft, P. L. Kaufman, K. S. Crawford, M. W. Neider, A. Glasser, and L. Z. Bito, “Accommodation dynamics in aging rhesus monkeys,” Am. J. Physiol. **275**(6 Pt 2), R1885–R1897 (1998).
45. M. Wojtkowski, A. Kowalczyk, R. Leitgeb, and A. F. Fercher, “Full range complex spectral optical coherence tomography technique in eye imaging,” Opt. Lett. **27**(16), 1415–1417 (2002).
46. M. Wojtkowski, R. Leitgeb, A. Kowalczyk, T. Bajraszewski, and A. F. Fercher, “In vivo human retinal imaging by Fourier domain optical coherence tomography,” J. Biomed. Opt. **7**(3), 457–463 (2002).
47. D. Zhu, M. Shen, H. Jiang, M. Li, M. R. Wang, Y. Wang, L. Ge, J. Qu, and J. Wang, “Broadband superluminescent diode-based ultrahigh resolution optical coherence tomography for ophthalmic imaging,” J. Biomed. Opt. **16**(12), 126006 (2011).
48. J. Jungwirth, B. Baumann, M. Pircher, E. Götzinger, and C. K. Hitzenberger, “Extended in vivo anterior eye-segment imaging with full-range complex spectral domain optical coherence tomography,” J. Biomed. Opt. **14**(5), 050501 (2009).
49. C. Kerbage, H. Lim, W. Sun, M. Mujat, and J. F. de Boer, “Large depth-high resolution full 3D imaging of the anterior segments of the eye using high speed optical frequency domain imaging,” Opt. Express **15**(12), 7117–7125 (2007).
50. H. Wang, Y. Pan, and A. M. Rollins, “Extending the effective imaging range of Fourier-domain optical coherence tomography using a fiber optic switch,” Opt. Lett. **33**(22), 2632–2634 (2008).
51. H. A. Lewis, C. Y. Kao, L. T. Sinnott, and M. D. Bailey, “Changes in ciliary muscle thickness during accommodation in children,” Optom. Vis. Sci. **89**(5), 727–737 (2012).
52. J. F. Koretz, C. A. Cook, and P. L. Kaufman, “Accommodation and presbyopia in the human eye. Changes in the anterior segment and crystalline lens with focus,” Invest. Ophthalmol. Vis. Sci. **38**(3), 569–578 (1997).
53. A. Glasser and P. L. Kaufman, “The mechanism of accommodation in primates,” Ophthalmology **106**(5), 863–872 (1999).
54. T. E. Lockhart and W. Shi, “Effects of age on dynamic accommodation,” Ergonomics **53**(7), 892–903 (2010).
55. J. A. Mordi and K. J. Ciuffreda, “Dynamic aspects of accommodation: age and presbyopia,” Vision Res. **44**(6), 591–601 (2004).
56. H. W. Jeong, S. W. Lee, and B. M. Kim, “Spectral-domain OCT with dual illumination and interlaced detection for simultaneous anterior segment and retina imaging,” Opt. Express **20**(17), 19148–19159 (2012).

1. Introduction

As a muscle-induced activity, accommodation in the human eye is a highly fluctuant and dynamic process. According to the classic accommodative theory of Helmholtz, the ciliary muscle contracts when accommodation occurs, causing the release of the zonular fibers, allowing the crystalline lens to increase curvature and thickness, and leading to an increase in the ocular refractive power to change the focus on a close target [1]. Initially, the ciliary muscle plays a role, while the crystalline lens serves as an effector in the process of accommodation. The capacity for accommodation declines with age, evidently due to the degeneration in both the elasticity of the crystalline lens and the activity of the ciliary muscle; this leads to presbyopia [2–7]. However, this theory may not fully explain the development of presbyopia. Investigating the crystalline lens response to ciliary muscle contraction may be beneficial to better understanding the aging problem. Nevertheless, the relationship between the crystalline lens response and ciliary muscle contraction has not been fully studied, mainly due to the technical difficulty of simultaneously imaging the anterior segment and the ciliary muscle in real-time.

Optical coherence tomography (OCT) is a non-contact, non-invasive imaging technology with a high resolution and high scan speed that has the capability to image both the anterior segment [8–11] and the ciliary muscle [12–14]. Swept-source OCT (SS-OCT), equipped with the high-speed reflective Fabry-Perot tunable lasers has been demonstrated to attain long image depths without the drop off in the sensitivity and the axial resolution versus depth [15–17]. Recently, using a custom tunable light source, SS-OCT has been demonstrated to have a unique performance for anterior segment imaging [18]. Using spectral domain OCT (SD-OCT) with two channels, a prolonged scan depth can be obtained for imaging the entire anterior segment [19,20]. Based on the previous work of our group [8,21] and that of others [22], the scan depth of the spectral domain OCT with a galvanometer-based switchable reference arm appeared to be sufficient for *in vivo* imaging of the ocular anterior segment through the pupil. Using a simple alternation of the reference arms, the entire anterior segment has been imaged by overlapping [8,21] or stitching [21,22]. Compared to our previous work [8,21], the long scan depth system used in the present study was optimized by improving the scan speed using complementary metal-oxide-semiconductor transistor (CMOS) technology. It is worth noting that these systems mentioned above are not capable of simultaneously imaging the anterior segment through the pupil and the ciliary muscle through the sclera. We combined the long scan depth system with another SD-OCT equipped with a light source centered at a wavelength of 1,310 nm to enable the assessment of the anterior segment including the ciliary muscle at different accommodative states. The goal of the present study was to demonstrate a novel approach of imaging the anterior segment including the ciliary muscle by combining two spectral domain optical coherence tomography devices.

2. Methods

2.1 Two SD-OCT devices

The improved system, which operates at 840 nm, was based on our previously reported long scan depth SD-OCT using a CCD camera [8,21]. The previous system demonstrated its suitability for imaging the entire anterior segment of the eye during accommodation [8,21]. The main benefit found in the improved system was the implementation of a CMOS camera to increase its scan speed for real-time imaging (Fig. 1). Briefly, a superluminescent diode (SLD, InPhenix, IPSDD0808, Livermore, CA, USA) with a central wavelength of 840 nm and the full-width at half bandwidths of 50 nm was used as the light source. The power output on the cornea was set to be 1.25 mW which was well below the safe cut-off value according to American National Standard Institute (ANSI) Z136.1. The spectrometer was composed of a collimating lens (f = 50 mm, OZ Optics, Ottawa, Canada), an 1800 lines/mm volume holography transmission grating, an image enlargement lens (Schneider, f = 240 mm, New York, NY), and a line array CMOS camera (Basler Sprint spL4096-140k; Basler AG, Germany). The acquisition speed of the camera was up to 70,000 A-lines/s, and the interference spectrum data were transferred using the image acquisition board (PCIe-1429, National Instruments, USA). The measured scan depth was 12.55 mm; the axial resolution of the system near the zero-delay line was approximately 7.0 μm in air; and the sensitivity was 99 dB near the zero delay line, with a 51 dB drop at the maximal imaging depth. The driver was developed in a setup with Labview (National Instrument, Austin, TX) running on a computer with Windows 7 (64 bit).

#180835 - $15.00 USD Received 10 Dec 2012; revised 14 Feb 2013; accepted 18 Feb 2013; published 21 Feb 2013

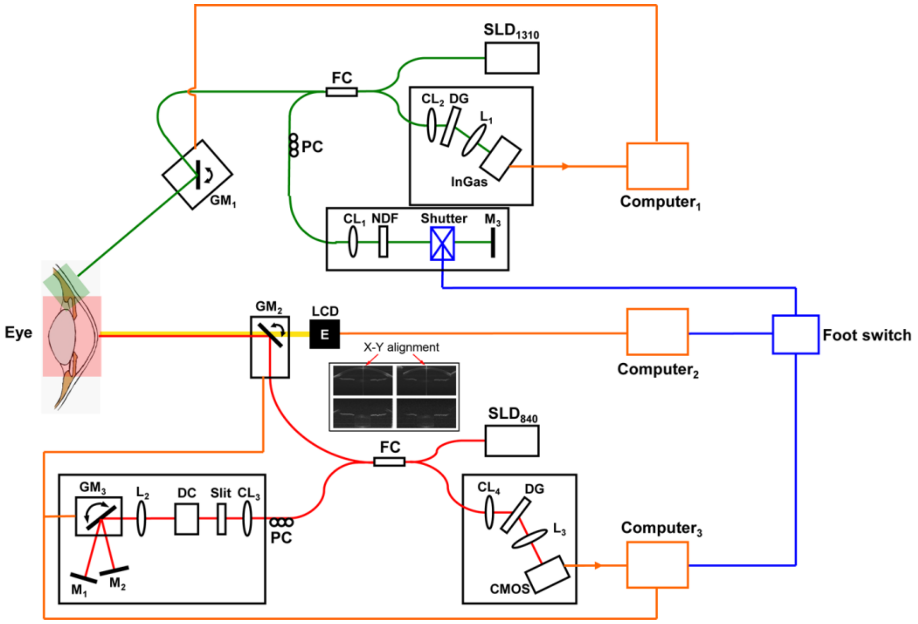

Fig. 1. Schematic diagram depicting the combined spectral-domain OCT systems. SLD$_{1310}$: superluminescent diode with a central wavelength of 1,310 nm, SLD$_{840}$: superluminescent diode with a central wavelength of 840 nm, FC: fiber coupler, PC: polarization controller, CL$_{1-4}$: collimating lenses, DC: dispersion compensator, L$_{1-3}$: objective lenses, M$_{1-3}$: refractive mirror, GM: galvanometer mirror, NDF: neutral density filter, LCD: liquid-crystal display, DG: diffraction grating, CMOS: complementary metal-oxide-semiconductor transistor camera, InGaAs: indium gallium arsenide. Insert: X-Y alignment.

The beam from the SLD was split into the sample arm and the reference arm using a 50:50 fiber coupler. In order to extend the effective image depth, the reference arm was specially designed, which consisted of two reflective mirrors (usually one reflective mirror in the reference arm). The two mirrors were mounted on two axial stages, respectively, which could adjust the optical path difference (OPD), amounting to two reference arms with different OPDs. Moreover, a galvanometer optical scanner with a silver mirror (GM in Fig. 1) was implanted in the reference arm, which could rapidly turn the beam between the two mirrors that was synchronized with the scanning. Thus a set of images that included the two frames was continually obtained during image acquisition. The difference in the OPD between the two mirrors was set about 11 mm, which was used to place the zero-delay lines of the two images on the top and the bottom of the anterior segment. Through image overlapping, the sensitivity drop was compensated, and the image enhancement was realized as described in our previous work [8,21]. This device (anterior segment OCT, AS-OCT) was used to image the entire anterior segment from the cornea to the crystalline lens through the pupil.

Another SD-OCT (CM-OCT) was used to image the ciliary muscle for acceptable penetration (Fig. 1). The spectrometer was custom-developed (Bioptigen, Durham, NC), and this device has been described elsewhere for imaging the anterior segment [23,24]. The light source was an SLD centered at a wavelength of 1,310 nm with a full-width at half maximum bandwidths of 75 nm. The output on the eye was set to 2.6 mW which was well below the ANSI safety limit for maximum permissible exposure of 15.4 mW at the wavelength [25]. In addition, most of the 1310 nm beam did not reach the retina because the iris blocked the light and the beam was directed to the limbal area. The scan depth was 3.8 mm with an axial resolution of ~8.0 μm in air. An indium gallium arsenide (InGaAs) camera (SU1024, Goodrich Sensors Unlimited Inc, Princeton, NJ) was used, and the system could image at 7 frames per second with an acquisition speed of 7,000 A-lines/s, corresponding to a frame of

1,000 A-lines. In real-time imaging, the images were continually acquired, processed and displayed. An electronic shutter (JML Optical, Rochester, NY) was implanted in the reference arm and used to insert a sync signal into OCT image acquisition during real-time imaging. The system ran with a proprietary program for data acquisition.

2.2 Combined sample arms and the synchronized real-time imaging

The sample arms of the two SD-OCT systems were combined and mounted on a slit-lamp microscope (Fig. 2). The probe of the AS-OCT was mounted on top of the slit-lamp microscope. A pair of X-Y galvanometers served as the scanner to image the anterior segment. Cross-hair scanning at the horizontal and the vertical meridians was used to align the scanning position of the eye by viewing the iris images in both horizontal and vertical images. The probe of the CM-OCT was placed on a translation stage that replaced the lamp holder of the slit-lamp. The platform of the stage had the capacity to rotate and vertically move, allowing a horizontal galvanometer to linearly scan the ciliary muscle at the temporal side through the sclera. The two beams were pre-aligned at the same altitude to cross at the corneal apex. The angle between the two probes was set at 30~50 degrees by moving the slit-lamp arms and rotating the stage platform. Both of the two beams from the two devices were focused on the sample by the objective lenses (f = 100 mm), which gave the lateral resolution of ~20 µm [10].

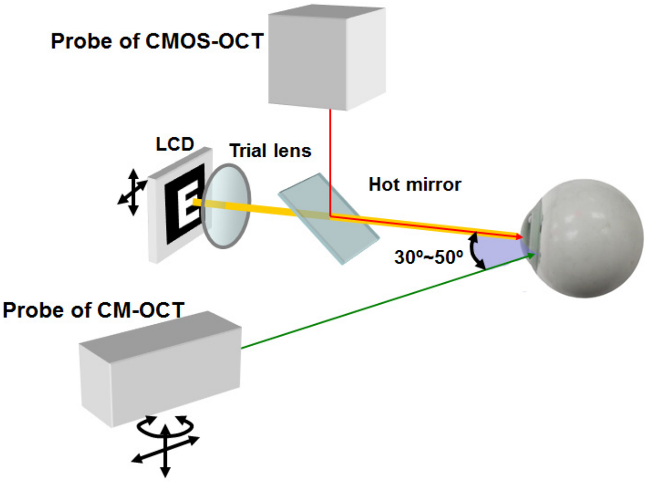

Fig. 2. Schematic diagram depicting the combination of the probes. LCD: liquid-crystal display.

To synchronize both sub-systems, a synchronization signal was needed to set the start point. We were not able to modify the proprietary software in the CM-OCT and the CM-OCT run during live view and the recording. If we stopped the recording during the alignment, we were not able to see the live view. Therefore, we implanted a shutter in the reference arm which provided the synchronization signal to the CM-OCT accounting as the start point. The acquisition of the AS-OCT was controlled by a foot switch that signaled the electronic shutter in the reference arm of the CM-OCT as described above (Fig. 1). The shutter, powered with a 5 volt direct current, could quickly block the light beam reflected in the reference arm. When the shutter closed at the onset of scanning, the detector of the CM-OCT did not receive the light from the reference arm, resulting in a blank frame without any information that served as a synchronization signal.

#180835 - $15.00 USD Received 10 Dec 2012; revised 14 Feb 2013; accepted 18 Feb 2013; published 21 Feb 2013

2.3 Accommodative module

A liquid-crystal display (LCD) screen showed a white Snellen letter “E” on a black background as the fixation target and was placed 10 cm from the tested eye. A trial lens combined with the LCD was used to compensate for the refractive error at close proximity and to stimulate the accommodation during image acquisition. The LCD and the trial lens were located on a translation stage with a dual axis for horizontal and vertical adjustments. The LCD was coupled with AS-OCT using a hot mirror (Fig. 2) and was synchronized with the acquisition of the OCT devices by the foot switch (Fig. 1) to alter the boundaries of the target between a blurred or sharp picture.

2.4 Participants and experiments

We performed two experiments using the combined system. A total of six subjects (5 male and 1 female, age range: 26 to 47 yrs) were included. This protocol was approved by the institutional review board for human research at the University of Miami. Informed consent was obtained from each subject, and all patients were treated in accordance with the tenets of the Declaration of Helsinki. In the first experiment, we imaged the left eye of each subject at two separate states. The refractive error during near vision of each subject was corrected by placing a trial lens with appropriate power into the fixation system. Subjects were asked to sit in front of the slit-lamp and to look forward at the letter “E”. In AS-OCT, the cross-hair alignment live view was used to align the iris image on both the horizontal and the vertical meridians so that the OCT beam was perpendicular to the iris plane (Fig. 1, Insert). In addition, the scan was centered on the apex as indicated by the specular reflex (the central vertical high reflectivity line on Figs. 3, 5 and 7; Media 1). During image acquisition, the operator adjusted the probe to ensure the beam from the AS-OCT pass through the corneal apex which ensured to scan the anterior segment at the same sagittal section. Before the experiment, the beam from the CM-OCT was pre-aligned with the beam from the AS-OCT at the same altitude. In addition, the specular reflex (vertical high reflectivity line) ensured sagittal scanning of the ciliary muscle (Figs. 4, 5 and 7; Media 2). After adjusting fixation to ensure the perfect alignment of the iris and corneal apex, the operator initiated the acquisition by stepping on the foot switch. Then, the equivalent accommodative stimulus of 4.00D was added to the trial lens, and the eyes were imaged following the same protocol. At each separate state, we repeated the exams twice. In this experiment, the ocular anterior segment at both the horizontal and the vertical meridian, which consisted of 2,048 × 4,096 pixels (lateral × axial) per frames with the scan speed of 17,500 A-lines per second, were imaged. Meanwhile, the ciliary muscle at the horizontal meridian of the temporal side was imaged at the scan speed of 7,000 A-lines per second; corresponding to the image size of 1,000 × 1,223 pixels (lateral × axial). Both of the OCT devices obtained 4 frames at each state, which took approximate 0.5 second.

In the second experiment, the left eye from a 26-year-old subject was imaged in real-time twice. The fixation target was blurred at first to fog the eye, and the picture was sharpened 1 second after the onset of the scanning to stimulate the accommodation. During the experiment, the subject was asked to keep the target as clear and sharp as possible. Sixty-two images, corresponding to thirty-one combined images of the anterior segment at the horizontal meridian, with 1,024 × 4,096 pixels (lateral × axial) per frame, were sequentially acquired using the AS-OCT in 3.72 seconds, with a single frame rate of 8.33 Hz. Meanwhile, the ciliary muscle at the temporal side was imaged using the CM-OCT at a frame-rate of 7 Hz. The starting point of the CM-OCT acquisition was one frame behind that of the AS-OCT because the first frame was uninformed. Thus, a total of 25 frames of the ciliary muscle were obtained over a total duration of 3.71 seconds.

#180835 - $15.00 USD   Received 10 Dec 2012; revised 14 Feb 2013; accepted 18 Feb 2013; published 21 Feb 2013

2.5 Image process and analysis

Figures 3A-3B show the two images and one combined image from the 26-year-old subject using the AS-OCT. The lateral scanning width was set to 15 mm. The zero-delay lines were set at the top and bottom of the two single frames, which were near the corneal apex and the posterior pole of the crystalline lens, respectively, with almost half of the dim images being due to a drop in the signal-to-noise ratio (SNR). An algorithm was developed and used to register the two images using the features in both of the images, such as the anterior segment of the lens and the iris. Briefly, the contour of the common portion, which included the surfaces of the iris and crystalline lens on the each frame, was extracted using segmentation algorithm based on the gradient information and shortest-path search and then converted to one dimensional curve. Then the transformation, which consisted of a combination of rotation and translation between the two frames according to the detected contours of the anterior surface of the iris and the lens, was used for the overlaying of the two frames. After registering and overlaying the images, the entire ocular anterior segment, including the cornea, iris, anterior chamber and crystalline lens, was clearly visualized in the combined image (Fig. 3C). Thus, the sensitivity drop was compensated for, and the enhancement of the anterior surface was realized.

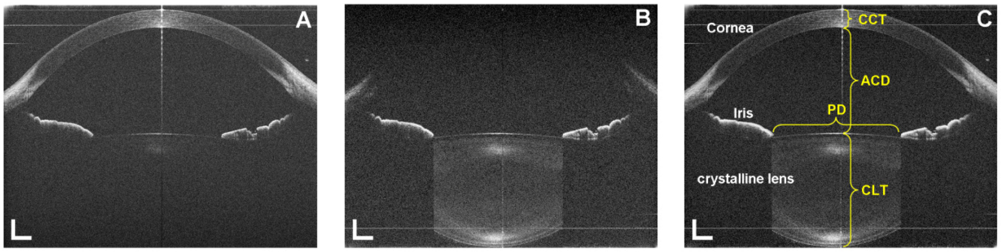

Fig. 3. Anterior segment from the cornea through the crystalline lens obtained from a 26-year-old subject. A: Frame 1 of the anterior segment; B: Frame 2 of the anterior segment; C: Combined image of the anterior segment. PD: pupil diameter; CCT: central corneal thickness; ACD: anterior chamber depth; CLT: central lens thickness. Bar = 1 mm.

The boundaries of the cornea and the crystalline lens were semi-automatically outlined using custom-developed software. Optical correction was performed based on Snell's principle. The correction approach has been well-documented in the literature [26–30], including in our previous work [8,31]. The refractive index of each medium (the refractive index of 1.387 for the cornea [32], 1.342 for the aqueous humor [33], and 1.408 for the crystalline lens [34]) at a wavelength of 840 nm was applied in the algorithm of correction. The central corneal thickness (CCT), the pupil diameter (PD), the anterior chamber depth (ACD), the curvature radii of the anterior (CAL) and posterior (CPL) lens surface, and the central lens thickness (CLT) were computed.

Overlaying multiple images for averaging was used to enhance the images of the ciliary muscle (Fig. 4). Four images were averaged. From the averaged images, the boundaries of the ciliary muscle, which defined as the intraocular boundaries of the sclera, the external edge of the pigmented ciliary epithelium and the internal edge of the iris, were manually segmented using custom developed software. After image correction for the optical distortion, the thickness of the ciliary muscle was evaluated by drawing lines through the points at 1 mm (CMT1) posterior to the scleral spur that were perpendicular to the local curvature of the sclera and extended to pigmented ciliary epithelium or the internal edge of the iris [12,35]. The thicknesses of the ciliary muscle at 2 mm (CMT2) and 3 mm (CMT3) posterior to the scleral spur and the maximum thickness of the ciliary muscle (CMTM) were calculated [12,35]. It is worth noting that the iris in the CM-OCT images (Figs. 4, 5 and 7) was shown as the flipped image. We put the OCT delay-line inside the eye (the bottom of the image) to improve the image quality of the ciliary muscle, resulting in the flipped iris image (as the conjugated artifact). The conjugated artifact is common in SD-OCT, unless phase shift method is used [20,36]. The conjugate artifact is not in time-domain OCT [35,37] or swept light source OCT [18]. The details of the conjugated artifact of the iris and its relation to the placement of the delay line have been reported in some published work [20,38]. The same phenomenon was shown in the attached video clips.

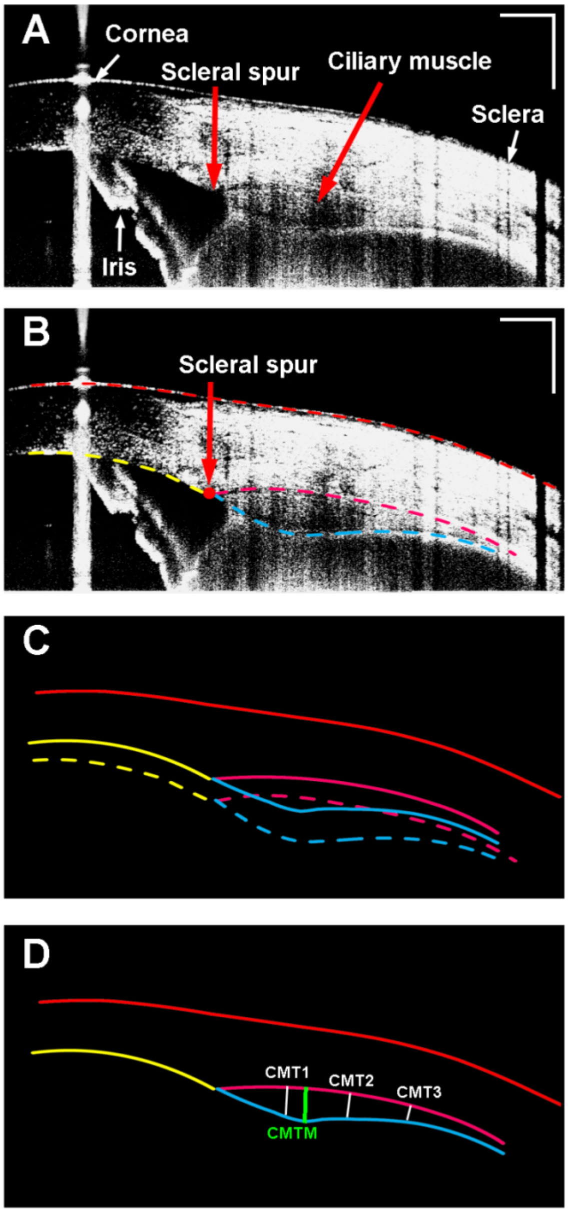

Fig. 4. Ciliary muscle obtained from a 26-year-old human subject. A: Enhanced image of the ciliary muscle; Note the iris was flipped as the mirror image due to placement of the zero-delay line inside the eye (bottom of the image). B: Semi-automatic segmentation of the boundaries of the cornea, the sclera, and the ciliary muscle. C: Optical correction for image distortion followed Snell's principle; D: The calculation of the ciliary muscle thickness. CMT1-3: the thickness of the ciliary muscle at 1 mm, 2 mm, and 3 mm posterior to the scleral spur; CMTM: the maximum thickness of the ciliary muscle. Bar = 1 mm.

#180835 - $15.00 USD   Received 10 Dec 2012; revised 14 Feb 2013; accepted 18 Feb 2013; published 21 Feb 2013

3. Results

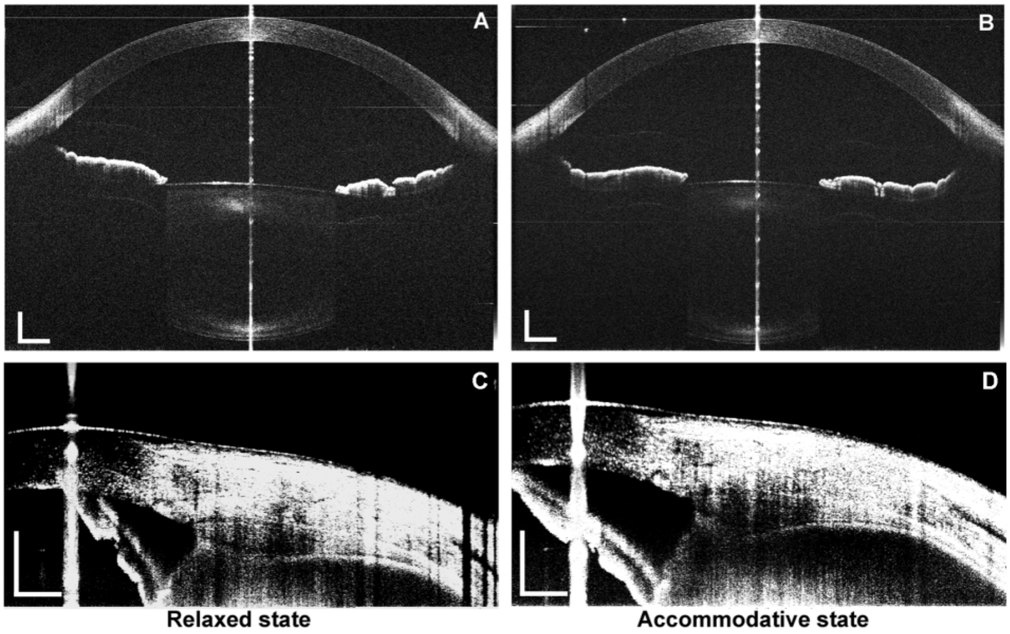

Fig. 5. The entire anterior segment (A and B) and the ciliary muscle (C and D) obtained from a 26-year-old subject using the combined devices in relaxed (A and C) and accommodative (B and D) states. The scan width of the anterior segment was set to 12 mm, with an image size of 2,048 × 4,096 pixels (lateral × axial), and to 10.3 mm for the ciliary muscle, with an image size of 1,000 × 1,223 pixels (lateral × axial). Bar = 1 mm. Note the iris (C and D) was flipped as the mirror image due to placement of the delay line inside the eye (bottom of the image).

Figure 5 shows the ciliary muscle and the anterior segment from the same subject before and after accommodation. Compared to the relaxed condition, pachynsis contraction was noted in the anterior portion of the ciliary muscle under accommodative condition. Although the thinning in the posterior part was not apparent in the figure, the averaged results from the study group showed significant thinning at the posterior portion of the ciliary muscle measured as the CMT3 (Fig. 6). In addition, changes in the anterior segment, including a thickening of the lens, a steepening in the lens surface, an increased shallowness in the anterior chamber depth, and the onset of miosis, were clearly observed. Figure 6 shows similar results between the two repeated measurements, as well as the biometric changes between the two states.

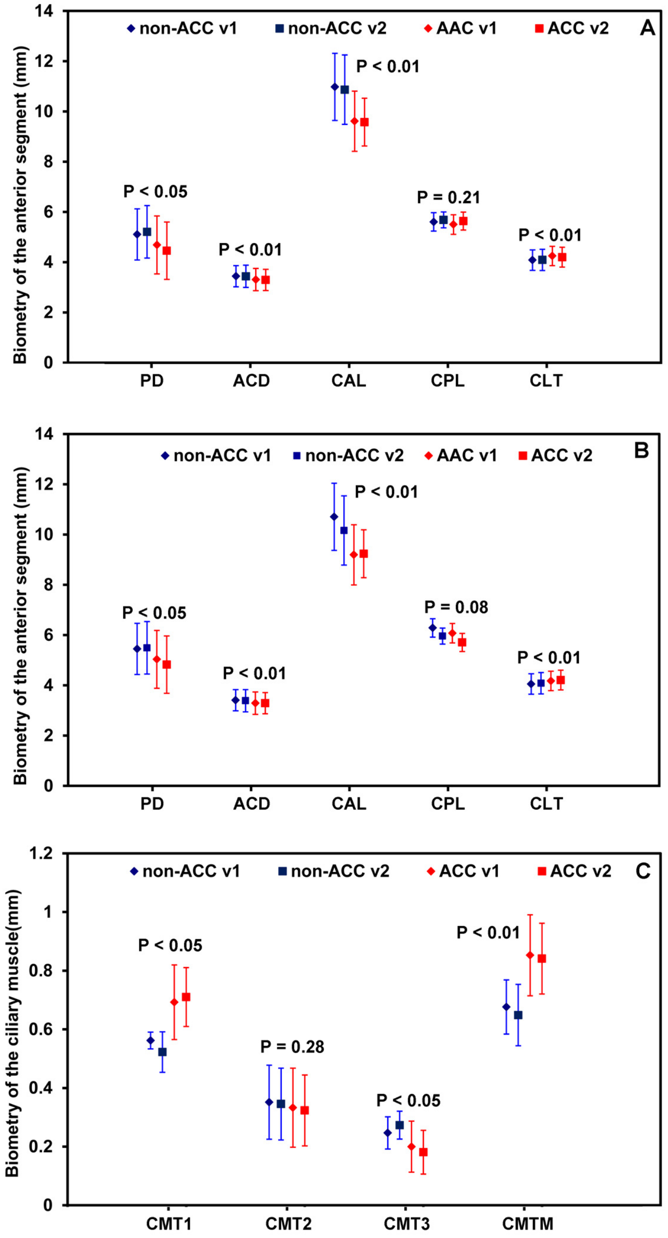

Fig. 6. Biometry of the anterior segment at the horizontal (A) and the vertical (B) meridians, as well as the ciliary muscle (C), within two visits during accommodation. PD: pupil diameter; ACD: anterior chamber depth; CAL: curvature radius of the anterior surface of the lens; CPL: curvature radius of the posterior surface of the lens; CLT: central lens thickness; CMT1-3: ciliary muscle thickness; CMTM: maximum thickness of the ciliary muscle. P value: difference of the mean values between the relaxed and the accommodative states. non-ACC: Relax status; ACC: Accommodative status; V1: visit 1; V2: visit 2.

Figure 7 shows the dynamic deformation of the ciliary muscle and the anterior segment in real-time. The biometric parameters of the lens and the ciliary muscle were calculated as the mean values before and after the accommodative stimulus onset, as shown in Table 1, and the dynamic changes calculated as the function of time are shown in Fig. 8. After the accommodative stimulus was given, the CMT1 and CMTM increased gradually, and reached the stable status at approximate 2 second (Figs. 8A and 8B, Table 1). Meanwhile, the CAL, PD and ACD decreased with the increasing in the CLT, and reached the accommodative status at approximate 2.5 second (Figs. 8C-8F, Table 1).

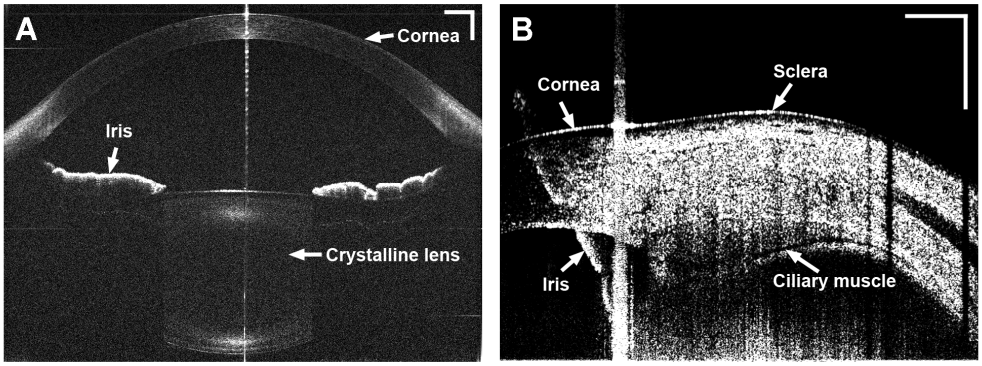

Fig. 7. Real-time display of the anterior segment (A) and the ciliary muscle (B) from a 26-year-old subject during 4.00D accommodation (Media 1 and Media 2). The frame rates of the movies were 8.33 fps (A) and 7 fps (B), respectively. Bar = 1 mm. Note the iris (B and Media 2) was flipped as the mirror image due to placement of the delay line inside the eye (bottom of the image).

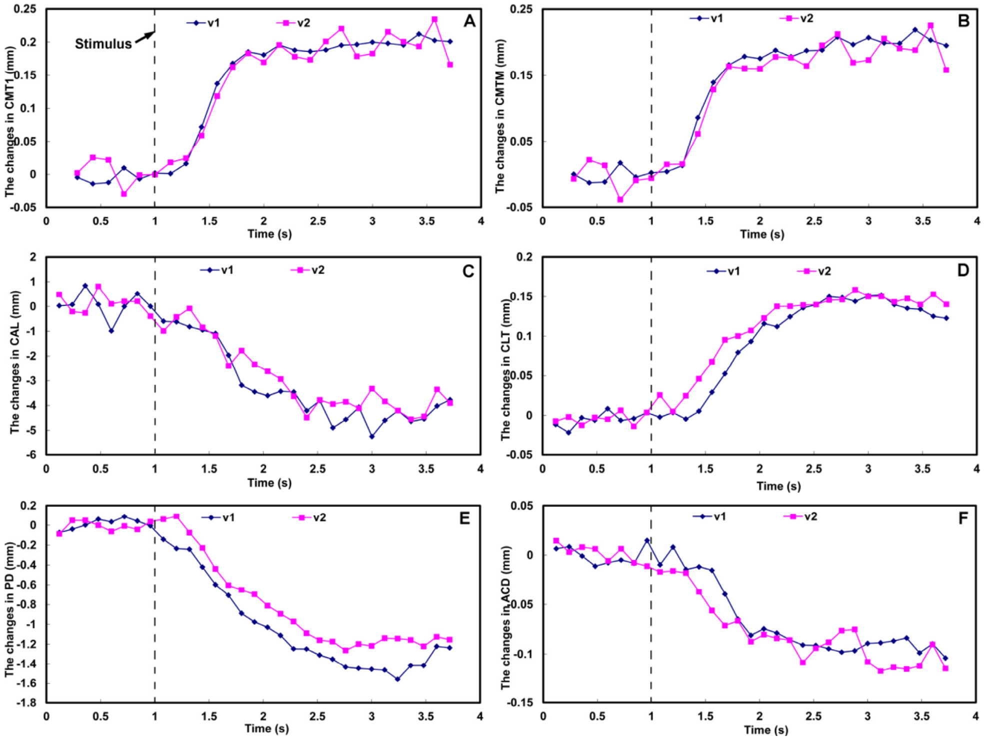

Fig. 8. Dynamics of the biometry of the ciliary muscle (A and B) and the anterior segment (C-F) during accommodation acquired at two visits (v1 and v2). Accommodative stimulus was set at 1 second after the start point of the scanning. CMT1: ciliary muscle thickness at 1 mm posterior to the sclera spur (A); CMTM: maximum thickness of the ciliary muscle (B); CAL: curvature radius of the anterior surface of the lens (C); CLT: central lens thickness (D); PD: pupil diameter (E); ACD: anterior chamber depth (F). V1: visit 1; V2: visit 2.

#180835 - $15.00 USD Received 10 Dec 2012; revised 14 Feb 2013; accepted 18 Feb 2013; published 21 Feb 2013

Table 1. The biometry of the ciliary muscle and the anterior segment before and after accommodation in a 26-year-old subject (unit: mm)

	Visit 1		Visit 2	
	0 D	4 D	0 D	4 D
Ciliary muscle				
CMT1	0.406 ± 0.009	0.605 ± 0.008	0.413 ± 0.020	0.603 ± 0.021
CMT2	0.279 ± 0.012	0.309 ± 0.011	0.290 ± 0.012	0.317 ± 0.014
CMT3	0.154 ± 0.008	0.151 ± 0.009	0.154 ± 0.009	0.162 ± 0.014
Maximum thickness	0.408 ± 0.011	0.606 ± 0.012	0.416 ± 0.021	0.604 ± 0.021
Crystalline lens				
Anterior surface curvature radius	12.05 ± 0.584	7.65 ± 0.464	11.72 ± 0.529	7.78 ± 0.387
Posterior surface curvature radius	5.82 ± 0.139	4.67 ± 0.313	5.53 ± 0.211	4.39 ± 0.327
Central thickness	3.62 ± 0.010	3.76 ± 0.010	3.63 ± 0.012	3.78 ± 0.006
Other biometry				
Pupil diameter	4.09 ± 0.061	2.70 ± 0.102	4.09 ± 0.054	2.91 ± 0.043
Anterior chamber depth	3.56 ± 0.008	3.47 ± 0.006	3.55 ± 0.010	3.45 ± 0.016
Central cornea thickness	0.55 ± 0.004	0.55 ± 0.006	0.56 ± 0.003	0.56 ± 0.006

CMT1-3: ciliary muscle thickness at 1 mm, 2 mm, and 3 mm posterior to the scleral spur.

The mean and standard deviation of the biometry at 0 D were calculated from 7 frames before the accommodative stimulus onset ($t < 1.0$ s).

The mean and standard deviation of the ciliary muscle thickness at 4 D were calculated from 13 frames after reaching the stable accommodative status ($t > 2.0$ s).

The mean and standard deviation of the crystalline lens and other biometry at 4 D were calculated from 11 frames after reaching the stable accommodative status ($t > 2.5$ s).

4. Discussion

Imaging the entire anterior segment has presented a substantial challenge. Strenk *et al.* developed high-resolution magnetic resonance imaging (MRI) for imaging the whole eye during accommodation to investigate the relationship between the ciliary muscle and the crystalline lens [39]. This technology offers direct visualization of the ciliary muscle and the lens periphery simultaneously without preventing visualization of the iris. This MRI has the disadvantage of a low spatial resolution (approximately 156 μm), which is roughly equivalent to the change in the maximum thickness of the lens and the ciliary muscle (approximate 100 to 200 μm) during accommodation. Time-consuming exams and high costs may limit its application to real-time imaging and to research on dynamic accommodation. Ultrasound biomicroscopy (UBM), which has good resolution (approximate 50 μm) and scan speed (more than 8 Hz), have been used to image the crystalline lens [40,41] and the ciliary muscle [42,43]. With this contact method, the configuration of the ciliary muscle was clearly visualized and the changes in the accommodative response could be documented. Moreover, with iridectomies in animal models, the ciliary process and the crystalline lens equator can be visualized using goniovideography [42,44]. These features cannot be visualized using OCT method if the iridectomy is not performed in human subjects.

Imaging the entire anterior segment from the cornea to the crystalline lens is difficult for SD-OCT due to the significant sensitivity decay with increased scan depth [8,22,45–47]. The decrease in the SNR with an increase in the imaging depth from the zero-delay line reduces the image contrast, causing the posterior portion of the lens to become unobservable [8,21,22]. With complicated phase shift technology, the entire anterior segment can be imaged by removing the complex conjugated image [36,38,48,49]. We previously imaged the anterior segment using a custom-built dual-channel dual-focus OCT system [19] that required two spectrometers and a 50% attenuation of the reflected light and resulted in a low-contrast image. Wang *et al.* extended the imaging range of an SD-OCT using a fiber optic switch in the reference arm, and this device has been demonstrated *in vitro* [50]. Using a fiber optic switch may require an additional patch fiber in the sample arm and possibly complicates the dispersion compensation [50]. As demonstrated in previous work by our researchers [8,21] and others [22], the use of a galvanometer to alter the reference arm length appears to be a simple and easy way to avoid the necessity for a patch fiber and adjustment of the dispersion compensation. Placing the zero delay line on the top of one image and on the bottom of the other image improves the SNR throughout the entire image depth and avoids possible conjugated artifacts. Therefore, image enhancement can be realized by the acquisition and overlapping of two frames. This technique is useful to extend imaging depths and to compensate for the sensitivity fall-off without eliminating complex ambiguity or reducing image contrast [8,21,22]. Additionally, this approach can further improve the scan depth by using more mirrors [22]. In the present study, we also improved our system by using a CMOS camera for a quicker scanning speed, and a similar design of overlapping images was utilized to extend the image range and to achieve real-time imaging of dynamic accommodation. The previous CCD-based approach had a limited scan speed and could not be used for real-time imaging [8,21]. Combining this improved system with our existing 1,310 nm SD-OCT enabled us to image the ocular anterior segment, including the cornea, anterior chamber, crystalline lens, and ciliary muscle.

Anterior segment OCT has been used to analyze the biometric changes of the ciliary muscle during accommodation [12–14,35,37,51]. Sheppard and Davies observed that the ciliary muscle showed a contractile shortening and a thickening in the anterior portion under the accommodative state [37]. Lossing combined an AS-OCT and an auto-refractor to investigate the relationship between the contraction of the ciliary muscle and the accommodative response [12]. In those studies, the measurements were taken at separate states, but not dynamically, mainly due to their slow scan speeds (approximately 2,000 A-lines/s) using time domain OCTs (TD-OCT) [12,13,37,51].

The custom-developed SD-OCT used in the present study improved the scanning speed for real-time imaging. In this static experiment, image enhancement was accomplished by averaging multiple images. The entire configuration of the ciliary muscle in non-human primate eyes has been previously documented using UBM [42,44], which could be used for imaging dynamic changes of the ciliary muscle. To the best of our knowledge, this is the first time that the dynamics of the ciliary muscle biometry on the human eye have been visualized by SD-OCT during accommodation. The combination of the two SD-OCT devices enabled the simultaneous imaging of the entire anterior segment. Due to the inaccessibility of the OCT software in the custom CM-OCT, the use of the synchronization marker in image recording may be an easy way to synchronize both systems. Further advances may involve data acquisition from two spectrometers with one computer, similar to the system used in the two-channel OCT system [19].

Our results on the biometry of the anterior segment obtained with this system are in agreement with the classic theories of Helmholtz [1] and others [2,7,52]. The deformation included a reduction of the pupil size, a shallow anterior chamber, a steep lens surface, an increased lens thickness [8,21,22], and a thickened anterior portion of the ciliary muscle, accompanied by a thinning in the posterior portion [12,13,37,51]. Further studies are required to investigate the relationship of the ciliary muscle and the crystalline lens with aging. Using UBM and goniovideography, Glasser *et al.* and Croft *et al.* imaged the lens, ciliary processes and the ciliary muscle in living monkeys that were undertaken surgical iridectomy during accommodation, which performed by stimulating the Edinger-Westphal (E-W) nucleus [42,44,53]. Although these studies were experimented in non-human primate eyes, the dynamic changes in the ciliary muscle and the crystalline lens during accommodation had been reported. In the present study, real-time imaging on the human eye *in vivo* was conducted and the dynamic accommodative responses of the ocular anterior segment, including the iris, crystalline lens and ciliary muscle were documented. Our results are in agreement with the previous findings obtained from non-human primate eyes. The findings in the present study were expected as the anatomy of the human and the monkey accommodative apparatus is very similar [42,44,53]. The combined system demonstrated an enhanced ability to understand dynamic accommodation. For instance, we found that the ciliary muscle started to contract 0.3 seconds after the accommodative stimulus was given and reached a stable state in approximately 0.5 seconds. The crystalline lens began to restore its shape following the contraction of the ciliary muscle, but its response ended later than that of the ciliary muscle. There was an approximate 0.5 second delay between the response times. This result implies that the deformation of the lens is slower than the contraction of the ciliary muscle. The similar finding of delayed responses was found in non-human primate eyes using UBM [44]. Early studies involving the reaction time of accommodative response found an age-related deterioration in dynamic accommodation [40,54,55]. The capacity to obtain real-time images of the response delay on the human eye using the non-contact OCT method may add an alternative modality for studying accommodation.

There are some limitations in the present study. The convergence, rotation and movements of the eye during accommodation may lead to errors in the dynamic measurements of the anterior segment biometry. The movies of the accommodative process showed minimal ocular movements. The small variability in the ocular biometry shown in Table 1 implies that the measurements are not seriously impacted by motion-related artifacts. However, the changes in the curvature radii of the lens surface showed more fluctuations, indicating that the lens shape may be more critically deteriorated by motion-related artifacts. The achievement of a 3D scanning pattern will require precise registration to avoid the influence of ocular movement in the future. Our current analysis for real-time imaging was processed by semi-automatic software that was extremely time-consuming. Automatic software for the registration, segmentation and calculation of these processes is being developed. Although our combined system is able to image the anterior segment including the ciliary muscle, the need to modify the reference arms for compensating sensitivity drop-off and implementation of the shutter may complicate the imaging approach. Further improvement with one system and alterative scanning channels [56] using the wavelength of 1 μm [18] may simplify the approach. Imaging the muscle apex position and width is important in studying the accommodative response. Apparently the image of the ciliary muscle obtained with OCT was not as clear as that obtained with UBM [42,43]. When the images were averaged, the configuration of the ciliary muscle appeared to be visualized as demonstrated in our 1st experiment, in which four images were averaged. Considering the non-contact feature and better resolution compared to UBM, OCT method may add an alternative tool for studying the real-time accommodative response, although OCT may not replace UBM in imaging the ciliary muscle. The image in the video was not as good as the averaged image because no averaging was applied in the real-time imaging. We did not overlay the images due to the limitation of the scan speed (7 Hz). Nevertheless, our approach would be a start to OCT real-time imaging of the ciliary muscle. In the future, high speed data acquisition with frame averaging may provide clearer visualization of the ciliary muscle in real-time.

In summary, we combined two custom-built spectral domain optical coherence tomography devices (SD-OCT) to simultaneously image the anterior segment and the ciliary muscle during accommodation. We also imaged dynamic changes of the anterior segment in one eye during accommodation. The combined systems provided the capacity for simultaneous, real-time imaging of the biometry of the anterior segment, including the ciliary muscle, *in vivo* during accommodation.

Acknowledgments

This study was supported by research grants from the NIH 1R21EY021336, NIH Center Grant P30 EY014801 and Research to Prevent Blindness (RPB).

#180835 - $15.00 USD Received 10 Dec 2012; revised 14 Feb 2013; accepted 18 Feb 2013; published 21 Feb 2013